PAPER

Spectral phase effects in above threshold ionization

To cite this article: A L Harris 2023 J. Phys. B: At. Mol. Opt. Phys. 56 095601

View the article online for updates and enhancements.

You may also like

- Influence of multi-photon excitation on the atomic above-threshold ionization Yuan-Ye Tian, , Chun-Cheng Wang et al.
- Dependence of above-threshold ionization spectrum on polarization directions of twocolor laser fields
 Min Liu, , Ying-Chun Guo et al.

- Angle-resolved photoelectron energy spectrum from the high-order above-threshold ionization process in IR+XUV two-color laser fields

Facheng Jin, Fei Li, Yujun Yang et al.

Spectral phase effects in above threshold ionization

A L Harris

Physics Department, Illinois State University, Normal, IL 61790, United States of America

E-mail: alharri@ilstu.edu

Received 19 December 2022, revised 28 February 2023 Accepted for publication 15 March 2023 Published 31 March 2023



Abstract

We present theoretical studies of above threshold ionization (ATI) using sculpted laser pulses. The time-dependent Schrödinger equation is solved to calculate the ATI energy and momentum spectra, and a qualitative understanding of the electron motion after ionization is explored using the simple man's model and a classical model that solves Newton's equation of motion. Results are presented for Gaussian and Airy laser pulses with identical power spectra, but differing spectral phases. The simulations show that the third order spectral phase of the Airy pulse, which can alter the temporal envelope of the electric field, causes changes to the timing of ionization and the dynamics of the rescattering process. Specifically, the use of Airy pulses in the ATI process results in a shift of the Keldysh plateau cutoff to lower energy due to a decreased pondermotive energy of the electron in the laser field, and the side lobes of the Airy laser pulse change the number and timing of rescattering events. This translates into changes to the high-order ATI plateau and intra- and intercycle interference features. Our results also show that laser pulses with identical carrier envelope phases and nearly identical envelopes yield different photoelectron momentum distributions, which are a direct result of the pulse's spectral phase.

1

Supplementary material for this article is available online

Keywords: above threshold ionization, sculpted laser pulse, Airy beam

(Some figures may appear in colour only in the online journal)

1. Introduction

One of the most instructive and valuable processes in attosecond and strong-field physics is that of above threshold ionization (ATI), in which an atom absorbs more photons than are required for ionization. The excess absorbed energy is converted to the kinetic energy of the ionized electron and the corresponding ATI spectrum has proven to be a valuable tool in many applications. In general, the ATI process can be largely understood using the three-step recollision model in which an electron is ionized and 'born' into the continuum (step 1), after which it accelerates in the electric field. When the electric field changes sign, it causes the electron to reverse direction (step 2) and recollide with the parent ion (step 3). If the electron is elastically scattered from the ion, it can then be accelerated again by the electric field before making its way to the detector. This leads to the so-called high-order ATI (HATI) electrons, which have been shown to be of use in reconstructing electron—ion scattering cross sections that contain target structure information [1–6]. HATI electrons are also used in the laser induced electron diffraction (LIED) technique, in which the recolliding electrons are used to probe the target structure with high temporal and spatial resolution [7–9]. Additionally, the ATI process can be used to characterize the carrier envelope phase (CEP) of the laser pulse, a quantity that is vital to accurately understanding processes involving few-cycle pulses [10].

Since the ATI process was first observed [11], there have been countless experimental and theoretical studies aimed at elucidating its dynamics and developing applications based on the process. Despite these decades of study, the ATI process still has insights to share. In this work, we combine the familiar ATI process with the use of temporally sculpted laser fields [12–17]. Unlike their more traditional sin-squared or Gaussian wave forms, temporally sculpted wave forms can have more complicated envelope functions with multiple peaks, carry quantized orbital angular momentum, or exhibit self-acceleration, self-healing, and limited diffraction [18–20].

To date, most studies of strong field physics with temporally sculpted pulses have used two-color laser fields [14, 15, 21], consisting of the fundamental field and one of its harmonics. By altering the relative phase between the two frequency components, the shape of the pulse envelope can be altered. Through an appropriate choice of relative phase and/or number of pulse cycles, signatures of intra- and intercycle interference can be observed in the photoelectron momentum distribution (PMD) [21]. Further analysis of the interference structures has been shown to reveal bound electron wave packet phase information [21] and the ability to resolve interference structures resulting from electron motion at the 100 as time scale [14].

Here, we present a theoretical study of ATI for hydrogen atoms using an alternative method of temporal envelope control. The laser pulse is chosen to be a few-cycle temporal Airy or Gaussian pulse. These pulses are carefully chosen such that they have identical power spectra, but different spectral phases. We aim to determine whether the spectral phase of the Airy pulse alters the photoelectron momentum and if this phase is imprinted on the photoelectron wave packet. If the temporally sculpted laser pulse alters the photoelectron wave packet, then the rescattering dynamics that lead to ATI and other higher order processes are also expected to change. The introduction of the Airy spectral phase as another control parameter in the ATI process could lead to new opportunities for examining target structures through LIED or generating higher order sculpted pulses via high harmonic generation (HHG).

We present numerical simulations of ATI for hydrogen using the time-dependent Schrödinger equation (TDSE) and combine this with analysis from the simple man's model (SMM) and a classical model in order to elucidate the effects of the sculpted laser field on the ionized electron dynamics. We show that the direct and rescattering plateau cutoffs in the ATI energy spectrum shift in energy for Airy pulses, and our classical simulations indicate that this shift can be traced to altered pondermotive energy and electron trajectories in the laser field following ionization. Additionally, we show that laser pulses with identical CEPs and nearly identical envelopes yield different PMDs, which are a direct result of the pulse spectral phase. The presence of the third order spectral phase alters the number and timing of ionization events, which results in a shift of the photoelectron's momentum.

The remainder of the paper is organized as follows. Section 2 contains the basic theoretical and numerical methods used. Section 3 presents the results along with a discussion of their significance. Lastly, section 4 provides a brief summary and outlook. Atomic units are used throughout unless otherwise noted.

2. Theory

2.1. TDSE

Because the primary dynamics of ATI with linearly polarized pulses happen along the laser polarization direction, a one-dimensional (1D) approximation is typically sufficient to capture the important physics. We note, however, that the high-order rescattering probability can be overestimated in a 1D compared to experiment and a full three-dimensional (3D) calculation, depending on the model potential used.

We solve the 1D TDSE for a single active electron atom in a laser field

$$\frac{i\partial}{\partial t}\psi(x,t) = \left[-\frac{1}{2}\frac{\mathrm{d}^2}{\mathrm{d}x^2} + V_{\mathrm{a}}(x) + xE(t) \right]\psi(x,t). \quad (1)$$

The atomic potential $V_a(x)$ is approximated with the pliant core model [22]

$$V_{\rm a}(x) = -\frac{1}{(|x|^{\alpha} + \beta)^{1/\alpha}}.$$
 (2)

Unlike the more familiar soft-core potential, the pliant core potential has a sharper cusp feature at the origin to more accurately model the electron's potential near the nucleus, while still asymptotically resembling the Coulomb potential far from the origin. A known feature of the soft-core potential is the underestimation of the spectral intensities by more than order of magnitude compared to 3D models. The pliant core potential corrects for this underestimation and has been shown to most reasonably approximate the results of a full 3D TDSE calculation for HHG [22] and ATI [23]. For the pliant core model, $\alpha=1.5$ and $\beta=1.45$ for hydrogen.

Two different temporal laser pulse fields E(t) are used: a Gaussian pulse and a truncated Airy pulse. The untruncated Airy function is a solution to the free particle Schrödinger equation [20] with infinite transverse extent and infinite energy (much like the plane wave). Alternatively, the truncated Airy pulse is a finite-width wave packet with finite energy and is a more reasonable model of a physical Airy laser pulse. Additionally, the truncated Airy pulse provides a tunable parameter ϕ_3 that can be used to adjust the shape of the envelope (see figure 1).

The Gaussian pulse is given by

$$E_{\rm G}(t) = E_0 e^{-2\ln 2\left(\frac{t-t_{\rm c}}{\Delta t}\right)^2} \sin\left(\omega_0\left(t-t_{\rm c}\right)\right) \tag{3}$$

and the truncated Airy pulse is given by [24]

$$E_{\rm A}(t) = E_0 \sqrt{\frac{\pi}{2 \ln 2}} \frac{\Delta t}{\tau_0} Ai \left(\frac{\tau - (t - t_{\rm c})}{\Delta \tau} \right) e^{\frac{\ln 2 \left(\frac{2\tau}{3} - (t - t_{\rm c}) \right)}{2\tau_{1/2}}} \times \sin \left(\omega_0 \left(t - t_{\rm c} \right) \right), \tag{4}$$

where $\tau_{1/2}$ is the exponential truncation half-life of the Airy, ω_0 is the carrier frequency, $\Delta \tau$ is the stretch of the Airy, Δt is

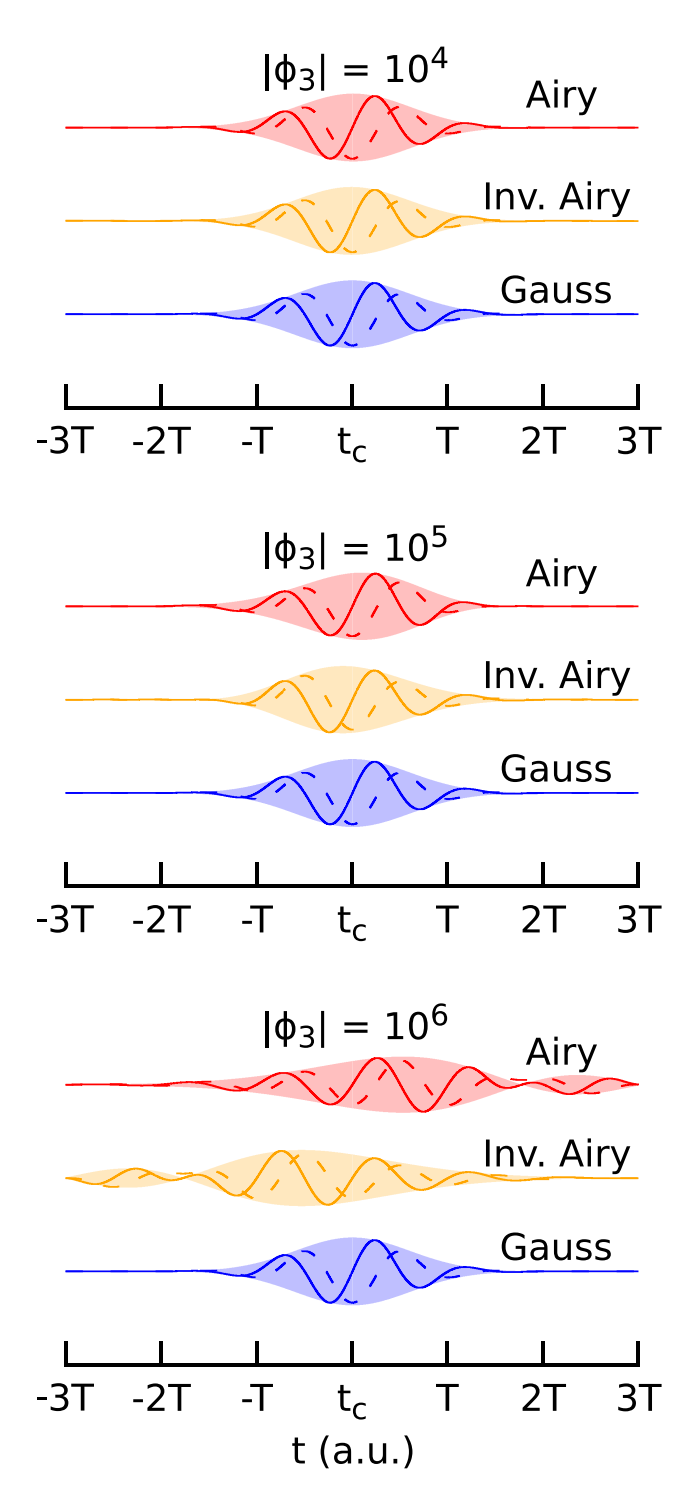


Figure 1. Temporal electric fields (solid lines) and vector potentials (dashed lines) for the six-cycle Airy and Gaussian laser pulses used in the calculations. The shaded areas represent the pulse envelope, and the vector potential has been scaled to have the same magnitude as the electric field. Pulse parameters were $\omega_0 = 0.057$ a.u. ($\lambda = 800$ nm), $E_0 = 0.0533$ a.u. ($I = 1 \times 10^{14}$ W cm⁻²), $\Delta t = 110$ a.u., $t_c = 330.5$ a.u. The third order phase terms ϕ_3 for the Airy and inverted Airy pulses are shown in the figure.

the full-width half-max (FWHM) of the temporal intensity, τ is the shift of the Airy, $t_{\rm c}$ is the center of the pulse, and $\tau_0 = \left(\frac{|\phi_3|}{2}\right)^{1/3}$ is a parameter related to the third order term ϕ_3 of

the spectral phase. The third order spectral phase controls the temporal envelope of the field and is related to the truncation half-life, stretch, and shift of the Airy by

$$\tau_{1/2} = \frac{2(\ln 2)^2 \phi_3}{\Delta t^2}$$
 (5)

$$\Delta \tau = \tau_0 \operatorname{sign}(\phi_3) \tag{6}$$

$$\tau = \frac{\Delta t^4}{32(\ln 2)^2 \phi_3}.\tag{7}$$

The vector potential can be calculated from the electric field by

$$A(t) = -\int_{-\infty}^{t} E(t') dt'.$$
 (8)

Figure 1 depicts the electric fields and vector potentials of the Airy and Gaussian pulses used here. As the magnitude of the third order spectral phase decreases, the Airy pulse envelope becomes more Gaussian-like and its width decreases. The number of side lobes of the Airy pulse also decreases with decreasing magnitude of the third order spectral phase. If ϕ_3 is negative, the orientation of the Airy pulse is reflected about its center. We refer to these pulses as inverted Airy pulses. It should be noted that the Gaussian, Airy, and inverted Airy pulses are identical with respect to CEP. Thus, the zeros of the electric field occur at the same instances in time, however the maximum and minimum of the electric field may occur at different instances and with different magnitudes based on the pulse envelope. Likewise, the zeros of the vector potentials for the different pulses occur at different times, which, as we discuss below, has important implications for the dynamics of the ionization.

A unique feature of the Gaussian and Airy pulses used here is that their spectral intensities are identical, and the frequency domain electric fields differ only by a phase. The Gaussian frequency domain electric field is

$$E_{\rm G}(\omega) = \frac{E_0 \Delta t \sqrt{\pi}}{2^{3/2} \sqrt{\ln 2}} e^{-\frac{\Delta r^2 (\omega_0 - \omega)^2}{(8 \ln 2)}}$$
(9)

and the Airy frequency domain electric field is [24]

$$E_{\mathcal{A}}(\omega) = E_{\mathcal{G}}(\omega) e^{-\frac{i}{6}\phi_3(\omega - \omega_0)^3}, \tag{10}$$

where ϕ_3 is the same third order term of the spectral phase as described above.

The pulses used here were truncated to include six cycles of the electric field. For values of $|\phi_3| \leq 10^5$, this truncation had no observable effect on the spectral intensity and the Gaussian, Airy, and inverted Airy pulses were nearly identical. However, for $|\phi_3| > 10^5$, the Airy and inverted Airy spectral intensities were altered as a result of the truncation and were no longer identical to that of the Gaussian pulse.

In solving the TDSE, the initial state atomic wave function was found by imaginary time propagation, and the 1D TDSE

was solved using the Crank–Nicolson method [25]. Absorbing boundary conditions [26] were used to prevent reflections from the grid boundary and the density of the wave function was checked at each time step to ensure that no probability was lost. The ATI energy spectrum was calculated using the window operator technique [27, 28]. All codes are available through figshare.com [29–31] and details of the numerical calculations are provided in appendix.

2.2. Semiclassical model

The dynamics of the ATI process for long laser pulses can be divided into two regimes: the Keldysh regime and the HATI regime. In the Keldysh regime [32], photoelectron kinetic energies are below approximately $2U_p$, where

$$U_{\rm p} = \frac{e^2 A_0^2}{4m} \tag{11}$$

is the pondermotive energy [33]. In this regime, the ATI electrons are a result of direct ionization in which the electrons make their way to the detector without further interaction with the parent ion. In the HATI regime, photoelectron kinetic energies are between $2U_p$ and $10U_p$. These photoelectrons result from the latter two steps of the three-step recollision model. Following ionization, the electron is accelerated by the electric field, which ultimately changes sign, causing the electron to reverse direction (step 2) and recollide with the parent ion (step 3). If the electron is elastically scattered from the ion, it can then be accelerated again by the electric field before making its way to the detector. The maximum kinetic energy of the rescattered electron occurs for the backscattering geometry, and classical momentum conservation yields a cutoff energy of approximately $10U_p$ [34].

Insight into the qualitative dynamics of the low energy ATI process can be found from using the SMM [35–39] within the strong field approximation (SFA) [35, 36]. Using the SFA, the transition amplitude of the electron from the bound state to the continuum state is written as [35, 36]

$$T_{fi} = -\sum_{i=1}^{2N} G\left[t_r^{(i)}, \vec{k}\right] e^{iS(t_r^{(i)})}, \tag{12}$$

where $t_r^{(i)}$ are the 2N release (ionization) times of the electron leading to a given final momentum \vec{k} for an N-cycle pulse, $G\left[t_r^{(i)}, \vec{k}\right]$ is the ionization amplitude,

$$S(t) = -\int_{t}^{\infty} dt' \left[\frac{(k+A(t'))^{2}}{2} + I_{p} \right]^{2}$$
 (13)

is the Volkov action, A(t) is the vector potential, and I_p is the ionization potential. The SMM uses a saddle point approximation of the SFA to find the release times such that

$$\frac{\partial S}{\partial t}|_{t_{\rm r}^{(i)}} = \frac{\left[k + A\left(t_{\rm r}^{(i)}\right)\right]^2}{2} + I_{\rm p} = 0. \tag{14}$$

This leads to complex values of the release times, since $I_p > 0$. However, in the SMM, I_p is assumed to be 0 and thus real-valued release times can be found from

$$k = -A\left(t_{\rm r}^{(i)}\right). \tag{15}$$

Therefore, within the SMM, the final momentum of the electron is predicted to be directly related to the vector potential at the electron's release time.

As shown in [40–42], the ATI process for few-cycle pulses can be viewed in the context of diffraction from a time grating where both intra- and intercycle interference features can be identified for *direct* electrons. The key to this interpretation lies in writing the PMD as a product of three terms [42]

$$P(k) \propto \Gamma(k) F(k) B(k)$$
, (16)

where $\Gamma(k)$ is the ionization rate, F(k) is the intracycle interference term, and B(k) is the intercycle interference term. The two interference terms can be written as

$$F(k) = \cos^2\left(\frac{\Delta S}{2}\right) \tag{17}$$

and

$$B(k) = \left| \sum_{j=1}^{N} e^{i\bar{S}_j} \right|^2, \tag{18}$$

where

$$\Delta S = S\left(t_{\rm r}^{(j,1)}\right) - S\left(t_{\rm r}^{(j,2)}\right) \tag{19}$$

is the difference in action between release times in the same cycle, and

$$\bar{S}_{j} = \frac{\left[S\left(t_{r}^{(j,1)}\right) - S\left(t_{r}^{(j,2)}\right)\right]}{2} \tag{20}$$

is the average action for release times in the same cycle. The index j indicates the pulse cycle, while the indices 1 and 2 denote early and late release times within the same cycle. These expressions apply to multicycle pulses with slowly varying envelopes. For the pulses used here, the envelope is not slowly varying, and in the case of the Airy and inverted Airy pulses, it is structurally complicated. Nonetheless, an analysis of these intra- and intercycle interference terms proves qualitatively insightful.

The ionization rate $\Gamma(k)$ decays with increasing momentum/energy and is responsible for the decrease of the ATI spectra with energy. The intracycle interference term F(k) results from the interference of two trajectories with release times in the same pulse cycle and provides an overall modulation to the spectrum. The intercycle interference term B(k) results from the interference between trajectories from N cycles of the pulse and leads to the well-known ATI peaks separated by energy $\hbar\omega$. In section 3, we present an analysis of the ATI energy spectrum and PMD for direct electrons in

the context of the time grating using the intra- and intercycle interference interpretation of the SMM.

For a qualitative understanding of the dynamics of rescattered electrons, we solved Newton's equation of motion for the classical trajectory of the electron in the laser field following ionization using the modified the ClassSTRONG program [43] From this, the kinetic energies of the direct and rescattered electrons were found as a function of ionization time. Additionally, the times of recollision and the classical trajectories are used to provide qualitative physical insight into the postionization electron dynamics for the different pulse types.

3. Results and discussion

3.1. ATI energy spectra

In general, the ATI energy spectrum for long laser pulses shows two distinctive plateaus that occur in regions of low and high energy. The first plateau appears in the Keldysh regime at low energy, and the second plateau is the HATI plateau, which occurs for high energy photoelectrons. The probability of HATI electrons is approximately the same for energies between 2 and $10U_{\rm p}$, leading to the HATI plateau. For long laser pulses, these plateaus are identifiable by relatively flat regions of the ATI energy spectrum that are followed by rapid decreases in photoelectron yield with increasing energy. For short pulses, the plateau regions are less distinct, but their cutoffs can still be identified as a maximum in photoelectron yield followed by a sharp drop of several orders of magnitude as energy increases.

Because the plateau cutoff energies are typically noted in units of pondermotive energy, an important consideration for short pulses is the variation of U_p with pulse cycle. By definition, the pondermotive energy is the cycle averaged electron kinetic energy in the laser field [44], and is given by the expression in equation (11) for long pulses. In this case, the vector potential for each cycle is approximately the same and the pondermotive energy does not change from one cycle to the next. However, for short pulses, the pulse intensity is different for each optical cycle, and therefore, the cycle-averaged energy is cycle-dependent. As was shown in [44], the pondermotive energy as a function of cycle number mirrors the pulse shape, with the pondermotive energy for a cycle in the middle of the pulse larger than that of a cycle near the edge of the pulse. Because the pondermotive energy is cycle-dependent, any predicted cutoffs in the ATI spectrum must consider this cycledependence. Our results show that the HATI plateau cutoff energy is shifted to significantly lower values for short pulses, and that using the maximum vector potential A_0 to calculate $U_{\rm p}$ does not accurately predict the HATI cutoff value. Additionally, for the different pulses used here, the maximum pondermotive energy varies with pulse type and this also affects the cutoff energy.

We performed calculations for an 800 nm laser pulse ($\omega_0 = 0.057$ a.u.) with intensity of $I = 1 \times 10^{14}$ W cm⁻² ($E_0 = 0.0533$ a.u.) and duration of 6 cycles. The pulse

had either a Gaussian or truncated Airy envelope with full-width half-max of $\Delta t = 110$ a.u., temporally centered at $t_c = 330.5$ a.u. Results are presented for Airy pulses with third order phase terms $10^4 \le |\phi_3| \le 10^6$.

Figure 2 shows the ATI energy spectra for a model hydrogen atom for Gaussian, Airy, and inverted Airy pulses. For the Gaussian pulse, the Keldysh and HATI plateaus are present, but their cutoff energies are shifted from their usual $2U_p$ and $10U_{\rm p}$ values. This is due to the relatively narrow pulse envelope, which effectively reduces the number of pulse cycles and limits rescattering. For the Airy and inverted Airy pulses with $|\phi_3| = 10^4$, the spectra are similar to that produced by the Gaussian pulse, which is expected since the electric fields are similar (see figure 1). As $|\phi_3|$ increases, the low energy ATI spectrum cutoff decreases, indicating that the direct electrons liberated by Airy or inverted Airy pulses gain less kinetic energy during their time in the laser field than those liberated by Gaussian pulses. This shift in low-energy cutoff can be traced to a decreased maximum electric field and vector potential of the Airy and inverted Airy pulses relative to the Gaussian pulses. For example, for $|\phi_3| = 10^6$, the maximum electric field strength of the Airy pulse is 83% of the maximum for the Gaussian pulse, and the vector potential maximum for the Airy pulse is 78% of the maximum vector potential for the Gaussian pulse. The reduced magnitude of the Airy and inverted Airy vector potentials causes a reduction in the pondermotive energy, which shifts the low-energy cutoff to smaller kinetic energies. Larger values of $|\phi_3|$ result in smaller values of the pondermotive energy and the cutoff shifts to even lower energy. These results are confirmed by the classical calculations shown below. The values of the pondermotive energies relative to the Gaussian pulse pondermotive energy are listed in table 1 for the different Airy and inverted Airy pulses used

3.2. Low energy electrons

At low energy, the ATI spectra show features of both intra- and intercycle interference. In figure 2, the intercycle ATI peaks are small due to the narrow pulse envelope that limits the number of non-negligible cycles to 1 or 2 (see figure 1). However, for the Airy and inverted Airy spectra with $|\phi_3| = 10^6$, additional intercycle interference structures are observed at low energy. These additional intercycle interference peaks can be traced to the additional non-negligible pulse cycles that are present for those pulses. The intercycle interference peaks are more readily seen in the PMD shown in figure 3(a), which shows the PMD as a function of momentum and laser pulse spectral phase. Data from the TDSE simulations are shown for $|\phi_3| \leq 10^5$, in which the pulse envelope resembles that of a Gaussian pulse and the ATI energy spectra at low energy for the different pulse types are similar. A clear change in the momentum distribution is observable as ϕ_3 changes, indicating that the spectral phase of the laser pulse can alter the photoelectron wave packet, despite nearly identical pulse envelope shapes. It is well-known that the CEP alters the PMD, despite

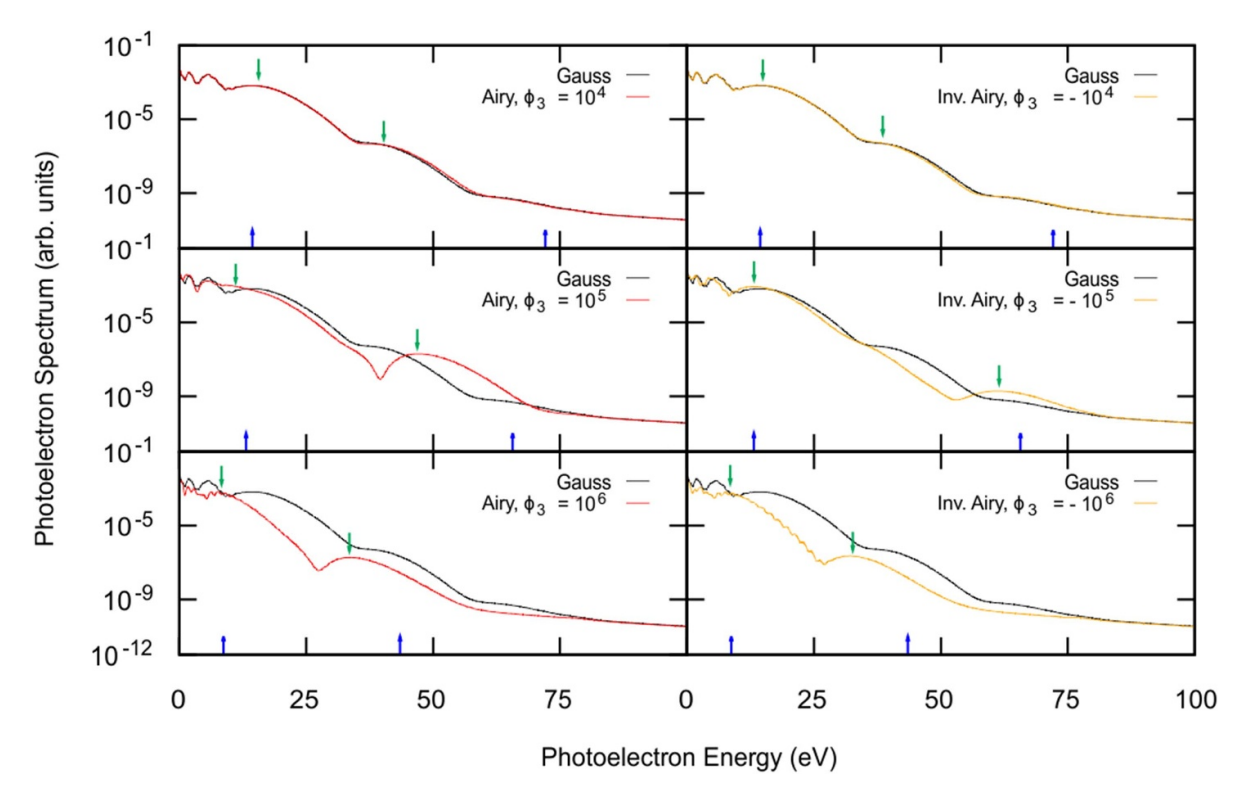


Figure 2. ATI photoelectron energy spectra for a hydrogen atom calculated with the 1D TDSE. The laser parameters are the same as figure 1. The black line is the spectrum for a Gaussian pulse (identical in all panels) and the red (orange) line is for a truncated Airy (inverted Airy) pulse. Third order phase values are listed in the figure. The blue arrows indicate the $2U_p$ and $10U_p$ values calculated using the maximum vector potential A_0 for each pulse type. The green arrows indicate the locations of the actual cutoffs in the spectra.

Table 1. Pondermotive energies relative to the Gaussian value for the Airy and inverted Airy pulses used in the calculations.

Pulse type	$U_{\rm p}$ relative to Gaussian $U_{\rm p}$
Gaussian	1
Airy/Inverted Airy $ \phi_3 = 10^4$	1
Airy/Inverted Airy $ \phi_3 = 10^5$	0.91
Airy/Inverted Airy $ \phi_3 = 10^6$	0.60

identical pulse envelopes. However, our results indicate that pulses with identical CEPs and nearly identical envelopes can still result in different PMDs as a result of altering the spectral phase. Figure 3(a) shows a nearly linear change in the most likely momentum value as ϕ_3 changes. As $|\phi_3|$ increases, the dominant momentum peak near zero splits into two peaks. For $\phi_3 > 0$, the dominant peak occurs at a positive momentum value, while for $\phi_3 < 0$, the dominant peak occurs at a negative momentum value.

The intercycle interference structures are readily seen in figure 3(a) and the absolute momentum of these intercycle interference peaks has an approximately linear dependence on ϕ_3 . The shift in momentum of the intercycle ATI peaks can be traced to two sources: the intracycle interference modulation and the relative time of electron ionization events between multiple cycles.

Consider first the intracycle interference that leads to the modulation of the ATI energy spectrum at low photoelectron energies. This modulation presents itself as multiple broad peak structures. As $|\phi_3|$ increases, the Airy and inverted Airy intracycle modulation peaks shift to lower energy relative to the Gaussian intracycle peaks. These shifts can be traced to the shifts in the F(k) term from the SMM which is shown in figures 4(a) and (b). To generate this figure, equation (15) was used to find release times for a final photoelectron momentum of 0.25 a.u. (i.e. A(t) = -0.25 a.u.). Figure 4(c) shows the vector potential for the Gaussian, Airy, and inverted Airy pulses with $|\phi_3| = 10^6$. Each time where the vector potential crosses the blue line at A(t) = -0.25 a.u. is a release time that leads to a final photoelectron momentum of 0.25 a.u. For the Gaussian pulse, there are two release times, while for the Airy and inverted Airy pulses with $|\phi_3| = 10^6$, there are 6 release times leading to this momentum. A similar analysis for $|\phi_3| = 10^5$ yields two release times for the Airy and inverted Airy pulses (not shown) when A(t) = -0.25 a.u. The release times found from the vector potentials show that the time difference between intracycle ionization events ($\Delta t = t_r^2 - t_r^1$) is different for Airy and inverted Airy pulses than that of the Gaussian pulse (see figure 4(c) inset). This difference in release times represents the time grating that leads to the diffraction effects seen in the ATI spectra and PMD. The smaller spacing of the intracycle time grating leads to an energy shift in the intracycle interference term that is shown in figures 4(a) and (b). This shift increases as $|\phi_3|$ increases. It has previously been shown [40] that changes to the intracycle modulation can alter the intercycle peak energies, and we conclude that this is one

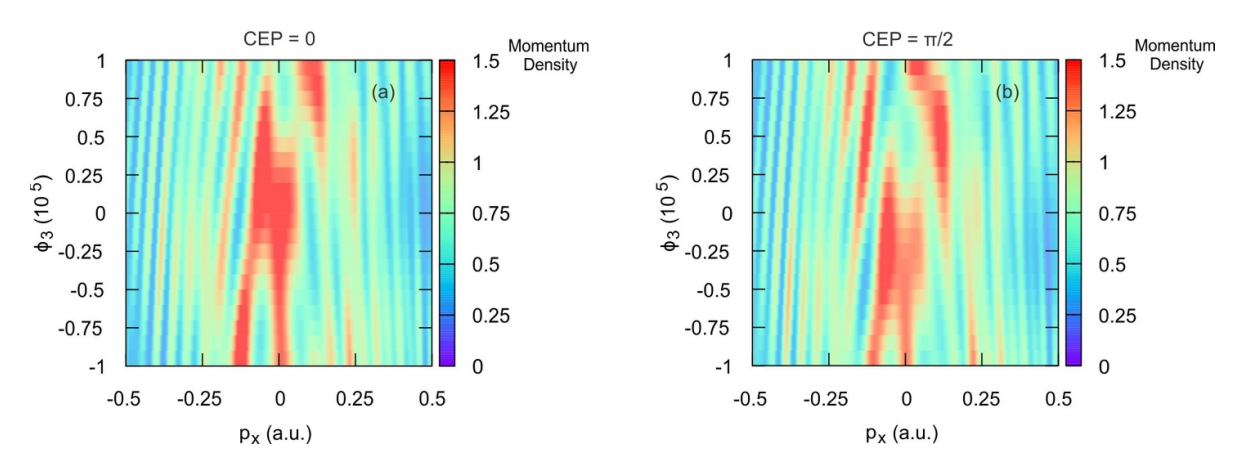


Figure 3. Photoelectron momentum distributions for ATI from hydrogen calculated using the time-evolved wave function from the 1D TDSE. The laser parameters are the same as figure 1. The momentum density (color) is plotted as a function of laser pulse spectral phase ϕ_3 and photoelectron momentum p_x . (a) CEP = 0 (b) CEP = $\pi/2$.

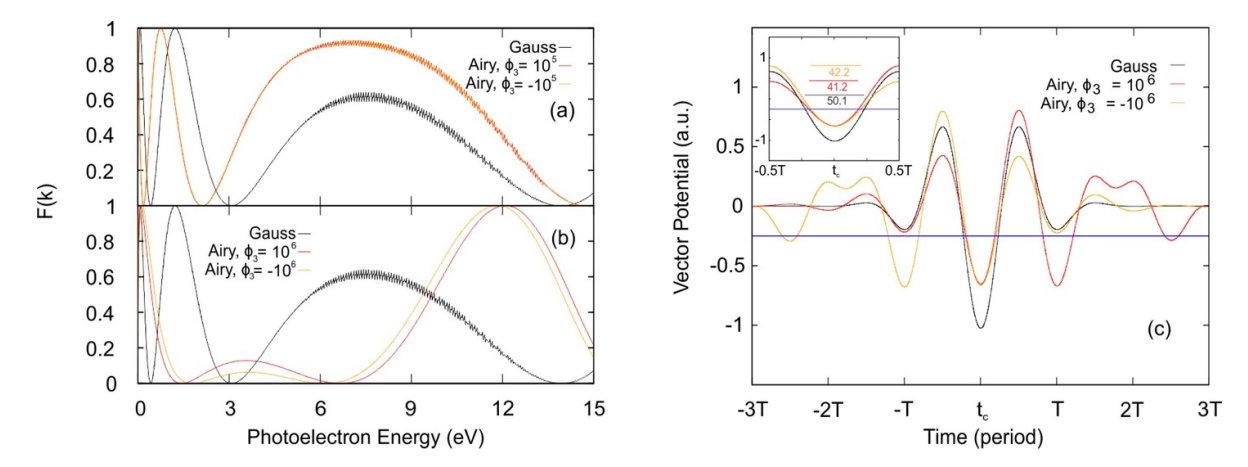


Figure 4. (a), (b) Intracycle interference term as defined in equation (17). Release times were found for a final photoelectron momentum of 0.25 a.u. (i.e. A(t) = -0.25 a.u.). (c) Vector potential for Gaussian, Airy, and inverted Airy pulses. Blue horizontal line denotes A(t) = -0.25 a.u. Inset of (c) shows the region near the center of the pulse, including intracycle release time differences ($\Delta t_{\text{Gauss}} = 50.1$ a.u., $\Delta t_{\text{Airy}} = 41.2$ a.u., $\Delta t_{\text{inverted Airy}} = 42.2$ a.u.).

source of the shift in intercycle interference peaks observed in the PMD of figure 3(a).

A second contributing factor to the shift of the intracycle interference peaks is the time difference between ionization events in different pulse cycles. Just as the third order phase of the Airy and inverted Airy pulses altered the time between intracycle ionization events it also changes the time between ionization events in consecutive cycles, as well as the number of cycles that lead to photoelectrons with a given momentum. This can again be seen in figure 4(c) where for A(t) = -0.25 a.u., the Airy and inverted Airy pulses have six release times (three cycles), but the Gaussian pulse has only two release times (one cycle). The change in release times and number of releases both contribute to alterations of the intercycle interference terms in the PMD. The additional release times at small values of |A(t)| result in the increased intercycle interference peaks at low energy in the ATI spectrum of figure 2 for $|\phi_3| = 10^6$.

For short pulses, the CEP is known to play a key role in the structure of the PMD and ATI energy spectra because the electric field becomes more asymmetric as the pulse duration decreases [10, 45]. This asymmetry shifts the vector potential, altering the intracycle and intercycle release times, which manifests as asymmetries in the PMD and energy spectra. Because the CEP can alter the electron trajectories after ionization, its control is relevant to the ATI process, as well as HHG. In this paper, in order to isolate the third order phase effects, we have focused on sculpted pulses with identical CEPs. A full analysis of CEP effects in sculpted Airy and inverted Airy pulses is beyond the scope of this paper, but we show in figure 3(b) the PMD for a CEP of $\pi/2$. A comparison of figures 3(a) and (b) shows that the interference pattern for CEP = 0 has shifted to smaller ϕ_3 values when the CEP = $\pi/2$. For example, the PMD for CEP = 0 and $\phi_3 \approx -0.5 \times 10^5$ occurs for CEP = $\pi/2$ at $\phi_3 \approx -0.8 \times 10^5$. This indicates that altering the third order phase has a similar effect as altering the CEP. It is likely that this is a result of the change in release times that occur as either CEP or ϕ_3 is changed. We plan future studies of CEP effects for sculpted Airy and inverted Airy pulses to elucidate a possible

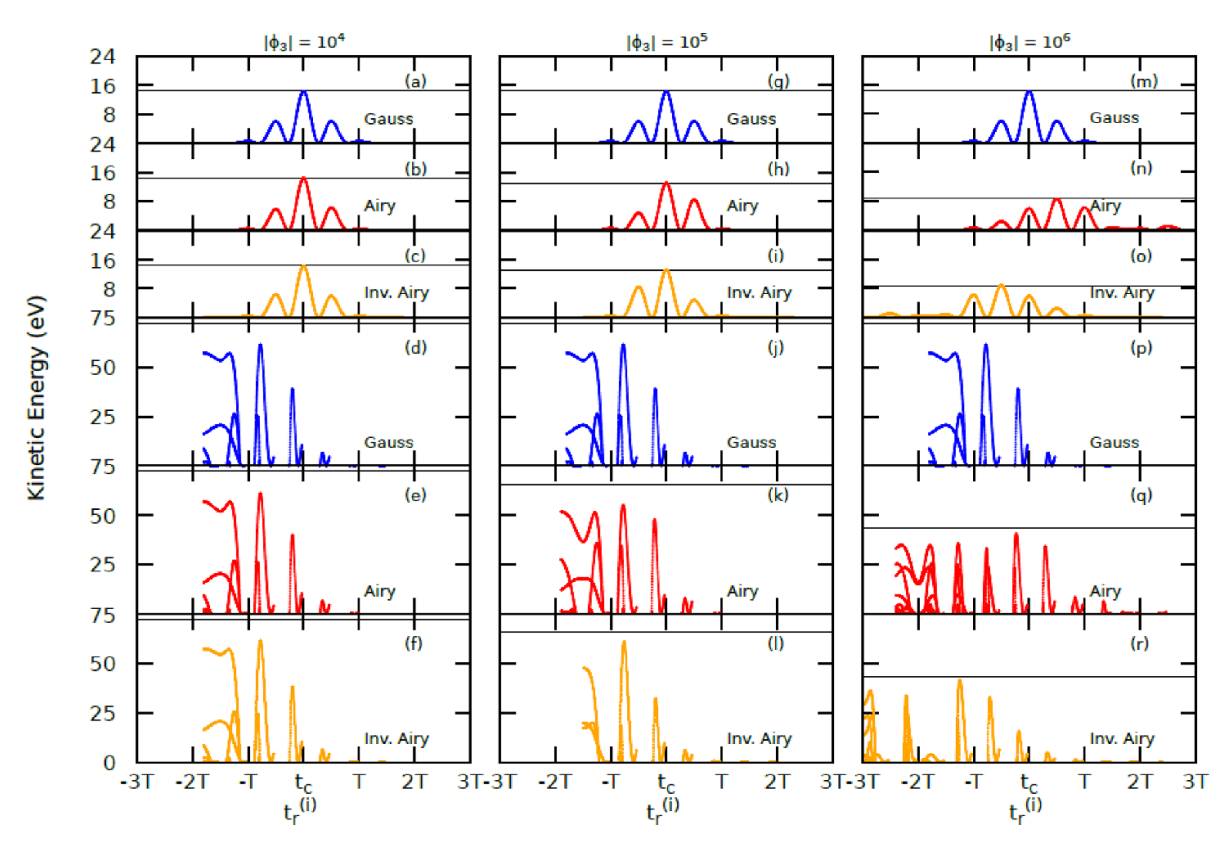


Figure 5. Kinetic energy spectra for direct (a)–(c), (g)–(i), (m)–(o) and rescattered (d)–(f), (j)–(l), (p)–(r) ATI electrons as a function of ionization time. Results were calculated with the classical model and $t_r^{(i)}$ is given in units of the electric field period (T=110~a.u.). The thin horizontal lines in each panel represent the $2U_p$ and $10U_p$ cutoffs adjusted for the different pulse types. Relative values of U_p for the pulses are listed in table 1.

connection between CEP effects and those of the third order spectral phase.

Further information about the dynamics of the electrons after ionization can be found by examining the classically predicted kinetic energy of the ionized electrons at the detector. As discussed above, direct electrons have a lower maximum kinetic energy than rescattered electrons and therefore, the kinetic energy can be used to separate direct and rescattered electrons. Figure 5 shows the classical prediction for the kinetic energy of the direct and rescattered electrons as a function of the release time. The thin horizontal lines in each panel represent the classically predicted $2U_p$ and $10U_p$ energy cutoffs calculated with A_0 for the different pulses. For direct electrons, the classical $2U_p$ cutoff value matches with the maximum kinetic energy of the direct electrons, indicating that the short pulse does not affect the kinetic energy.

The laser pulse shape has a clear effect on the shape of the kinetic energy spectrum for the direct electrons, particularly for large $|\phi_3|$. The maximum in the direct electron kinetic energy spectrum coincides with the maximum of the pulse envelope and therefore, the direct electrons with the largest kinetic energy are produced at earlier times for the inverted Airy pulse and later times for the Airy pulse. The kinetic energy spectrum of direct electrons produced by Airy and inverted Airy pulses is also asymmetric with respect to the pulse's temporal center. The peak value of the electric field envelope is shifted to later times for the Airy pulse

and earlier times for the inverted Airy pulse. This asymmetry causes the electrons ionized by the Airy pulse after the temporal center to have greater kinetic energy than those ionized before, while the opposite is true for the inverted Airy pulse. The direct electron kinetic energy spectrum also shows the multiple peak structure of the pulse envelopes when $|\phi_3|=10^6$. The secondary lobe of the Airy pulse results in the production of direct electrons at later ionization times that are not present for the Gaussian or inverted Airy pulse. Likewise, the inverted Airy pulse produces earlier direct electrons that are not present with the Gaussian or Airy pulses.

3.3. High energy electrons

At high energy, the HATI plateau cutoff is observable in the Gaussian pulse ATI spectrum at approximately 40 eV. For the Airy pulses, this plateau cutoff shifts in energy and magnitude depending on the value of ϕ_3 . For $\phi_3 > 0$, the HATI plateau cutoff shifts to larger energies when $\phi_3 = 10^5$, and maintains its magnitude. For $\phi_3 = 10^6$, the HATI plateau cutoff shifts to lower energies and decreases in magnitude. For the inverted Airy pulse, the HATI plateau cutoff shifts to much larger energies at $\phi_3 = -10^5$ and decreases significantly in magnitude. However, for $\phi_3 = -10^6$, the HATI plateau cutoff resembles that of the Airy pulse, occurring at lower energies and with a reduced magnitude.

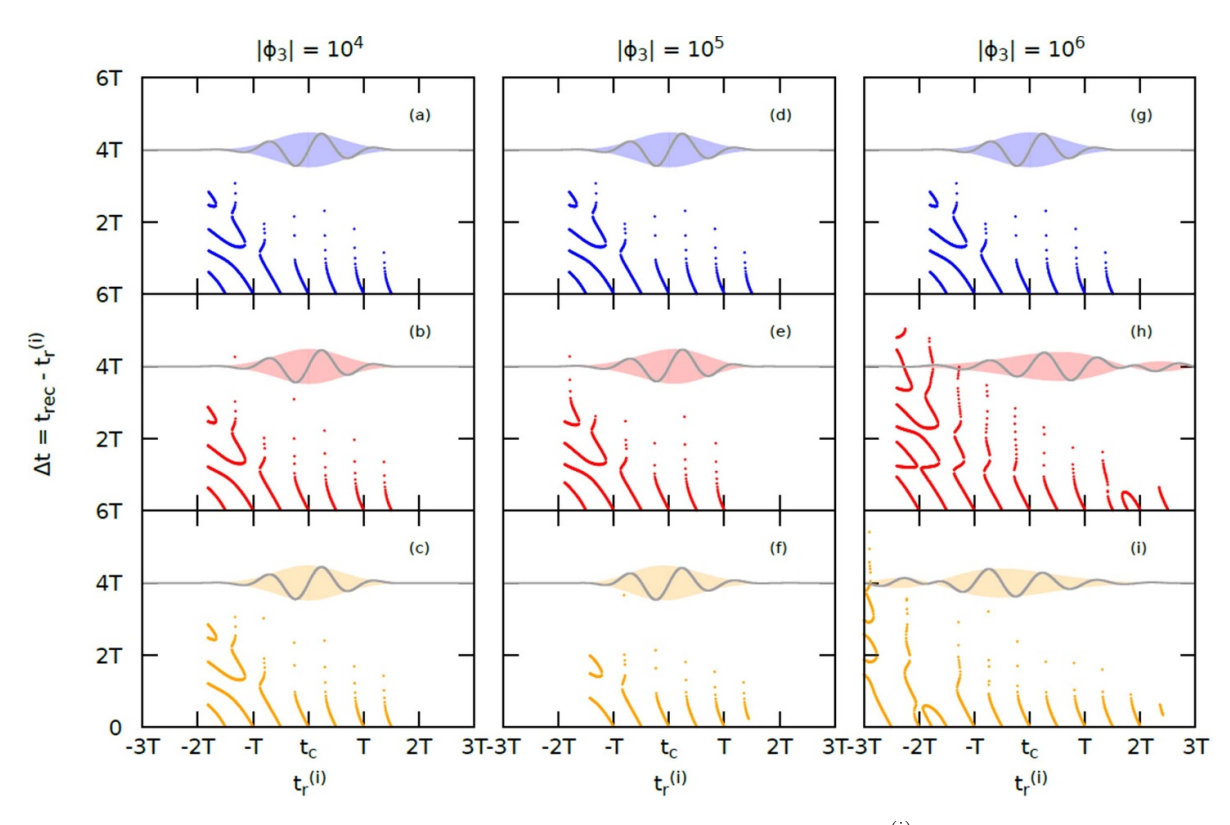


Figure 6. Time difference Δt between ionization and recollision as a function of ionization time $t_r^{(i)}$ calculated with the classical model. Each data point represents a recollision event. Times are in multiples of the electric field period (T = 110 a.u.) and t_c is the temporal center of the pulse ($t_c = 330.5$ a.u.). The electric fields are shown in each panel along the horizontal line at 4 T. The third order spectral phase is listed at the top of each column for the Airy and inverted Airy pulses, and the Gaussian plots in (a), (d), (g) are identical.

By solving Newton's equation of motion for an electron in an oscillating electric field [43], the times of recollision (t_{rec}) as a function of release time ($t_r^{(i)}$) can be found. If the oscillating electric field drives the electron back to the parent ion, its position will return to the origin, and the time that this occurs is defined as the recollision time. It is possible that the electron returns to the origin at multiple instances as it is forced back and forth in the electric field, in which case there are multiple recollision times for a single release time.

Figure 6 shows a plot of the time difference between ionization and recollision Δt (i.e. time after ionization) as a function of release time for the three pulse types. A single point on the graph indicates a $(t_r^{(i)}, \Delta t)$ pair and a higher location of the point on the vertical axis indicates that the recollision occurs later after ionization. Because it is unlikely that an electron is ionized when the pulse strength is negligible, we show only $(t_r^{(i)}, \Delta t)$ pairs for when the electric field is greater than 1% of E_0 . A vertical line drawn through the plot reveals that the number of Δt values for a given $t_r^{(i)}$ (i.e. vertical line crossings) equals the number of recollisions for a given ionization time. In all cases, there are more recollisions for electrons ionized earlier in the pulse than later in the pulse. This is expected given that the later an electron is ionized, the fewer cycles of the electric field it experiences, and thus the fewer recollisions.

Figure 6 shows that the different pulse shapes lead to different recollision dynamics after ionization. For the inverted Airy pulse, there are fewer recollisions because the leading side lobes cause an increased electric field strength at earlier times. This enhanced electric field is able to drive the electron sufficiently far away from the origin that even the strong oscillations caused by the main lobe are too weak to bring the electron back to the parent ion. As $|\phi_3|$ increases, this effect is enhanced and fewer rescattering events are observed. These dynamics are expected to result in direct electrons coming from earlier ionization events and overall fewer rescattered electrons for the inverted Airy pulse, a result that is confirmed in the analysis of electron kinetic energies shown in figure 5.

In contrast, electrons ionized by the Airy pulse experience additional recollisions at later times compared to the Gauss and inverted Airy pulses. These additional recollisions are caused by the trailing side lobe of the Airy pulse, which enhances the electric field at later times relative to the Gaussian or inverted Airy pulses. This increased field strength at later times drives additional recollisions. Again, as $|\phi_3|$ increases, this effect is enhanced and more rescattering events are observed. In the case of the Airy pulse, the post-ionization dynamics are expected to result in fewer overall direct electrons and more rescattering at later ionization times, a result that is also confirmed in the kinetic energy spectra of figure 5.

As discussed above, the laser pulse envelope affects the electron release times and alters the kinetic energy spectrum of direct electrons. The same is true for the kinetic energy

spectrum of the rescattered electrons, with most differences again observed for the largest $|\phi_3|$ value. Unlike the direct electrons, the kinetic energy of the rescattered electrons is less than the classically predicted $10U_p$ maximum value. As $|\phi_3|$ increases, the predicted kinetic energies approach the $10U_{\rm p}$ value. This is a result of the additional recollisions that occur for pulses with large $|\phi_3|$ values. For the Gaussian and Airy or inverted Airy pulses with small $|\phi_3|$, there are very few recollisions due to the short pulse duration, and thus the maximum possible kinetic energy is less than $10U_p$. For $|\phi_3| = 10^6$, more recollisions are possible and the maximum kinetic energy of the rescattered electrons increases. Specifically, as was shown in figure 6, the Airy pulse produces electrons that undergo more rescatterings, than those produced by the inverted Airy and Gaussian pulses. The increased number of rescatterings by electrons ionized early from an Airy pulse leads to greater kinetic energy of these electrons compared to those ionized by a Gaussian pulse at the same time. Additionally, the trailing second lobe of the Airy pulse for $|\phi_3| = 10^6$ leads to rescattered electrons with higher kinetic energy produced at later times than those of a Gaussian pulse.

For the inverted Airy pulse with $|\phi_3| = 10^6$, the emission of electrons that undergo rescattering occurs in two groupings, corresponding to the two lobes of the pulse envelope. The initial lobe is present for $t_{\rm r}^{(i)} < -2{\rm T}$ and leads to electrons that rescatter with lower kinetic energy. This is followed by a second lobe for $t_{\rm r}^{(i)} > -2{\rm T}$, which leads to the second set of electrons that rescatter with higher kinetic energy. The rescattered electrons ionized later by the inverted Airy pulse gain more kinetic energy than those ionized at the same times by the airy pulse, a direct effect of the pulse envelope asymmetry.

4. Summary

By solving the TDSE, we have calculated ATI spectra for hydrogen in the presence of sculpted laser fields. Results were compared for electrons ionized by Gaussian, Airy, and inverted Airy pulses with identical power spectra. These calculations showed that the Keldysh plateau cutoff was shifted to lower energy when either an Airy or inverted Airy pulse was used. This shift was due to the reduced vector potential magnitude, which reduced the pondermotive energy. The third order spectral phase was also shown to alter the timing of intracycle ionization events, which affected the intracycle interference modulation in the ATI energy spectra. The low energy PMD was also affected by the third order spectral phase, despite the pulses having identical CEPs and nearly identical envelopes. Additionally, the intercycle interference of low energy electrons was altered by the third order spectral phase through a change in number and timing of ionization events across multiple cycles.

For rescattered electrons, the HATI plateau cutoff energy shifted to either higher or lower values for the Airy and inverted Airy pulses as a result of changes in rescattering dynamics. Using a classical model, we showed that for the Airy pulse, there were more recollisions at later times due to the trailing side peaks of the pulse. In contrast, for the inverted Airy pulse,

there were overall fewer recollisions due to the leading side lobes of the pulse causing ionization that drove the electron far from the origin. The number of recollisions affected the maximum possible kinetic energy of the photoelectron, and consequently led to the observed changes in the ATI energy spectrum.

Given that the ATI process is ubiquitous in ultrafast physics, the results presented here provide qualitative and quantitative insight into the effect of temporally sculpted laser pulses on the dynamics of the ATI process. The presence of the third order spectral phase term in the complex electric field spectrum of the Airy pulse provides an additional control parameter for tuning the temporal field, while maintaining the spectral intensity. Our results provide evidence that the photoelectron momentum and energy are altered through changes to the laser pulse spectral phase, as are the dynamics of ATI photoelectrons. It is therefore expected that future investigations of highorder processes using Airy pulses will result in changes to the dynamics of these processes. These results lay the groundwork for applications of sculpted laser pulses in processes such as high order harmonic generation, non-sequential double ionization, streaking, RABBITT, and the attoclock.

Data availability statement

All data that support the findings of this study are included within the article (and any supplementary files).

Acknowledgments

We gratefully acknowledge the support of the National Science Foundation under Grant No. PHY-2207209.

Appendix

A. TDSE

The 1D TDSE was solved using the Crank–Nicolson method [25]. The initial state wave function was evolved from t=0 to t=661 a.u. (the end of the laser pulse) with a time step of 0.01 a.u. The spatial grid spanned from -3000 a.u. to 3000 a.u. with a step size of 0.033 a.u. Absorbing boundary conditions were employed [26] in the form of a mask function that prevented unphysical reflections at the boundaries

$$g(x) = \cos^{1/8}\left(\frac{\pi(|x| - (x_{\text{max}} - 50))}{2(50)}\right),$$
 (A1)

where x_{max} is the boundary edge (i.e. 3000 a.u.). At each time step, the wave function within 50 a.u. of the boundary (i.e. x < -2950 a.u. or x > 2950 a.u.) was multiplied by g(x).

B. Initial state wave function

The initial state atomic wave function was found by imaginary time propagation using an algorithm similar to that of

the Crank–Nicolson method. The time step was 0.01 a.u. The spatial grid spanned from -500 a.u. to 500 a.u. with a step size of 0.1 a.u. The initial guess of the wave function was [46]

$$\psi(x,0) = (1 + \sqrt{x^2 + 1}) e^{-\sqrt{x^2 + 1}}.$$
 (A2)

C. Window method

The ATI energy spectrum was calculated using the window operator technique [27, 28]. The energy bin width was $2\gamma = 0.02$ and the integer power for the window operator was n = 2.

D. Classical calculations

The classical calculations for finding the recollision times and kinetic energies of the direct and rescattered electron were calculated using a modified version of the ClassSTRONG program [43]. Simulations for the recollision times were run from t = 0 to a final time of t = 661 a.u. with 1000 time steps. For the kinetic energies, the simulations were run from t = 0 a.u. to t = 661 a.u. with 7000 time steps.

ORCID ID

A L Harris https://orcid.org/0000-0003-2689-982X

References

- [1] Milošević D B, Becker W, Okunishi M, Prümper G, Shimada K and Ueda K 2009 Strong-field electron spectra of rare-gas atoms in the rescattering regime: enhanced spectral regions and a simulation of the experiment *J. Phys. B: At. Mol. Opt. Phys.* **43** 015401
- [2] Gaarde M B, Schafer K J, Kulander K C, Sheehy B, Kim D and DiMauro L F 2000 Strong species dependence of high order photoelectron production in alkali metal atoms *Phys. Rev. Lett.* 84 2822–5
- [3] Okunishi M, Morishita T, Prümper G, Shimada K, Lin C D, Watanabe S and Ueda K 2008 Experimental retrieval of target structure information from laser-induced rescattered photoelectron momentum distributions *Phys. Rev. Lett.* 100 143001
- [4] Ray D et al 2008 Large-angle electron diffraction structure in laser-induced rescattering from rare gases Phys. Rev. Lett. 100 143002
- [5] Morishita T, Le A-T, Chen Z and Lin C D 2008 Accurate retrieval of structural information from laser-induced photoelectron and high-order harmonic spectra by few-cycle laser pulses *Phys. Rev. Lett.* 100 013903
- [6] Chen Z, Le A-T, Morishita T and Lin C D 2009 Quantitative rescattering theory for laser-induced high-energy plateau photoelectron spectra *Phys. Rev.* A 79 033409
- [7] Meckel M et al 2008 Laser-induced electron tunneling and diffraction Science 320 1478–82
- [8] Zuo T, Bandrauk A D and Corkum P B 1996 Laser-induced electron diffraction: a new tool for probing ultrafast molecular dynamics Chem. Phys. Lett. 259 313–20
- [9] Lein M, Marangos J P and Knight P L 2002 Electron diffraction in above-threshold ionization of molecules *Phys. Rev.* A 66 051404

- [10] Sayler A M, Rathje T, Müller W, Rühle K, Kienberger R and Paulus G G 2011 Precise, real-time, every-single-shot, carrier-envelope phase measurement of ultrashort laser pulses Opt. Lett. 36 1–3
- [11] Agostini P, Fabre F, Mainfray G, Petite G and Rahman N K 1979 Free-free transitions following six-photon ionization of xenon atoms *Phys. Rev. Lett.* 42 1127–30
- [12] Frederick N J, Victor B M and Charles F F 1974 Dislocations in wave trains *Proc. R. Soc.* A 336 165–90
- [13] Siviloglou G A, Broky J, Dogariu A and Christodoulides D N 2007 Observation of accelerating Airy beams *Phys. Rev.* Lett. 99 213901
- [14] Arbó D G, Nagele S, Tong X-M, Xie X, Kitzler M and Burgdörfer J 2014 Interference of electron wave packets in atomic ionization by subcycle sculpted laser pulses *Phys. Rev.* A 89 043414
- [15] Schumacher D W, Weihe F, Muller H G and Bucksbaum P H 1994 Phase dependence of intense field ionization: a study using two colors *Phys. Rev. Lett.* 73 1344–7
- [16] Muller H G, Bucksbaum P H, Schumacher D W and Zavriyev A 1990 Above-threshold ionisation with a two-colour laser field J. Phys. B: At. Mol. Opt. Phys. 23 2761
- [17] Ehlotzky F 2001 Atomic phenomena in bichromatic laser fields *Phys. Rep.* 345 175–264
- [18] Voloch-Bloch N, Lereah Y, Lilach Y, Gover A and Arie A 2013 Generation of electron Airy beams *Nature* 494 331–5
- [19] Siviloglou G A and Christodoulides D N 2007 Accelerating finite energy Airy beams *Opt. Lett.* **32** 979–81
- [20] Berry M V and Balazs N L 1979 Nonspreading wave packets Am. J. Phys. 47 264–7
- [21] Xie X *et al* 2012 Attosecond probe of valence-electron wave packets by subcycle sculpted laser fields *Phys. Rev. Lett.*108 193004
- [22] Silaev A A, Yu R M and Vvedenskii N V 2010 Strong-field phenomena caused by ultrashort laser pulses: effective oneand two-dimensional quantum-mechanical descriptions *Phys. Rev.* A 82 033416
- [23] Tian Y-Y, Li S-Y, Wei S-S, Guo F-M, Zeng S-L, Chen J-G and Yang Y-J 2014 Investigation on the influence of atomic potentials on the above threshold ionization *Chin. Phys.* B 23 053202
- [24] Wollenhaupt M, Assion A and Baumert T 2007 Femtosecond laser pulses: linear properties, manipulation, generation and measurement Springer Handbook of Lasers and Optics ed F Träger (New York: Springer) pp 937–83
- [25] Press W H, Vettering W T, Teukolsky S A and Flannery B P 1992 Numerical Recipes in Fortran (Cambridge: Cambridge University Press)
- [26] Krause J L, Schafer K J and Kulander K C 1992 Calculation of photoemission from atoms subject to intense laser fields *Phys. Rev.* A 45 4998–5010
- [27] Schafer K J and Kulander K C 1990 Energy analysis of time-dependent wave functions: application to above-threshold ionization *Phys. Rev.* A 42 5794–7
- [28] Schafer K J 1991 The energy analysis of time-dependent numerical wave functions *Comput. Phys. Commun.* 63 427–34
- [29] Harris A L 2022 tdse.cn.f (https://doi.org/10.6084/m9.figshare. 21084826)
- [30] Harris A L 2022 ati.spectrum.1d.f (https://doi.org/10.6084/m9. figshare.21084841)
- [31] Harris A L 2022 imaginary.time.prop.f (https://doi.org/10. 6084/m9.figshare.21084808)
- [32] Frolov M V, Manakov N L and Starace A F 2009 Analytic formulas for above-threshold ionization or detachment plateau spectra *Phys. Rev.* A 79 033406
- [33] Becker W, Goreslavski S P, Milošević D B and Paulus G G 2018 The plateau in above-threshold ionization: the

- keystone of rescattering physics J. Phys. B: At. Mol. Opt. Phys. 51 162002
- [34] Paulus G G, Becker W, Nicklich W and Walther H 1994 Rescattering effects in above-threshold ionization: a classical model J. Phys. B: At. Mol. Opt. Phys. 27 L703–8
- [35] Lewenstein M, Kulander K C, Schafer K J and Bucksbaum P H 1995 Rings in above-threshold ionization: a quasiclassical analysis *Phys. Rev.* A 51 1495–507
- [36] Lewenstein M, Balcou P, Yu I M, L'Huillier A and Corkum P B 1994 Theory of high-harmonic generation by low-frequency laser fields *Phys. Rev.* A 49 2117–32
- [37] Corkum P B, Burnett N H and Ivanov M Y 1994 Subfemtosecond pulses *Opt. Lett.* **19** 1870–2
- [38] Chirilă C C and Potvliege R M 2005 Low-order above-threshold ionization in intense few-cycle laser pulses *Phys. Rev.* A 71 021402
- [39] Ivanov M, Corkum P B, Zuo T and Bandrauk A 1995 Routes to control of intense-field atomic polarizability *Phys. Rev.* Lett. 74 2933–6
- [40] Arbó D G, Ishikawa K L, Schiessl K, Persson E and Burgdörfer J 2010 Diffraction at a time grating in above-threshold ionization: the influence of the Coulomb potential *Phys. Rev.* A 82 043426

- [41] Arbó D G, Ishikawa K L, Persson E and Burgdörfer J 2012 Doubly differential diffraction at a time grating in above-threshold ionization: intracycle and intercycle interferences Nucl. Instrum. Methods Phys. Res. B 279 24–30
- [42] Arbó D G, Ishikawa K L, Schiessl K, Persson E and Burgdörfer J 2010 Intracycle and intercycle interferences in above-threshold ionization: the time grating *Phys. Rev.* A 81 021403
- [43] Ciappina M F, Pérez-Hernández J A and Lewenstein M 2014 ClassSTRONG: classical simulations of strong field processes Comput. Phys. Commun. 185 398–406
- [44] Della Picca R, Gramajo A A, Garibotti C R, López S D and Arbó D G 2016 Nonconstant ponderomotive energy in above-threshold ionization by intense short laser pulses *Phys. Rev.* A 93 023419
- [45] Rathje T, Johnson N G, Möller M, Süßmann F, Adolph D, Kübel M, Kienberger R, Kling M F, Paulus G G and Sayler A M 2012 Review of attosecond resolved measurement and control via carrier–envelope phase tagging with above-threshold ionization J. Phys. B: At. Mol. Opt. Phys. 45 074003
- [46] Majorosi S, Benedict M G and Czirják A 2018 Improved one-dimensional model potentials for strong-field simulations *Phys. Rev.* A 98 023401